Element partitioning during carbonated pelite melting at 8, 13 and 22 GPa and the sediment signature in the EM mantle components

Daniele Grassi [a], Max W. Schmidt [a,*], Detlef Günther [b]

[a] Department of Earth Sciences, ETH, 8092 Zurich, Switzerland
[b] Department of Chemistry and Applied Biosciences; ETH, 8093 Zurich, Switzerland

ARTICLE INFO

ABSTRACT

Within the subducting oceanic crust, carbonated eclogitic pelites are the lithology with the lowest melting temperature at >5 GPa, i.e. at depths beyond major subarc dehydration. 200–400 °C below the oceanic mantle geotherm, carbonated pelites generate alkali-rich Ca-carbonate melts that constitute efficient metasomatic agents of the mantle. Partition coefficients between residual minerals and such melts were experimentally determined at 8, 13, and 22 GPa at 1100–1500 °C. Compared to previous studies, clinopyroxenes have higher jadeite contents (57–82 mol%) resulting in a larger compatibility for LILE. In garnet, the compatibility of REE increases from incompatible LREE ($D_{La} \sim 0.005$ at 8–22 GPa) to slightly compatible Lu ($D_{Lu} = 0.96$ to 3.5 at 8–22 GPa), D_{HFSE}'s increase with pressure from slightly incompatible at 8 GPa to highly compatible at 22 GPa, always with $D_{Hf} > D_{Zr}$. K-hollandite/carbonate melt partition coefficients at 13 GPa are all <0.3 except for K itself. At 22 GPa, Rb, Sr, Ba, and Pb also become compatible in K-hollandite. Also at 22 GPa, FeTi-perovskites appear and have high D-values for HFSEs (D_{HFSE} 28–88), similar to other Ti-rich minerals. In the CAS phase, also occurring at 22 GPa, Ti, Sr, La to Gd, and Pb, Th and U are compatible ($D_{Pb} > D_{Th} > D_U > 1.7$ with a D_{Pb}/D_U of 12 to 26) leading to a strong fractionation of these elements during melting just above the 660 km discontinuity.

Calculated bulk residue/carbonate melt partition coefficients increase with pressure for almost all elements. At 22 GPa, i.e. for carbonated sediment melting in the transition zone, element fractionation strongly effects the Pb isotopic evolution. Carbonate melt trace element compositions normalized to primitive mantle show strong enrichments in incompatible elements including LILE and LREE and relative negative anomalies for Ti at 8 and 13 GPa and for Hf, Zr and Ti at 22 GPa at which pressure absolute values are close to mantle concentrations. Primitive mantle normalized patterns for 8 GPa carbonate melts are similar to ultrapotassic rocks and many lamproites on one hand confirming the involvement of a sedimentary component in the source region of these rocks, on the other hand defining this component as a carbonated sediment melt. The melting of mantle domains re-enriched by ~0.4 wt.% of our 8–13 GPa carbonate melts produces the typical trace element signature observed in the group II kimberlites. Finally, the Pb, Nd, and Sr isotopic evolution of mantle domains contaminated by ≤ 1 wt.% carbonate melt derived from carbonated pelites yields reservoirs which cover most of the compositions identified as EM I and II flavors in OIBs.

© 2012 Elsevier B.V. All rights reserved.

1. Introduction

Within a subducting slab carbonated pelites are the lithology with the lowest solidus temperature at >5–7 GPa, i.e. at pressures beyond major dehydration at subarc depths (Grassi and Schmidt, 2011a,b). Combined with their position at the top of a slab stratigraphic column, this renders them the first lithology of the subducting oceanic crust to melt during crustal recycling into the mantle at 170 to ≥ 660 km depth. Furthermore, solidus temperatures 200–300 °C below the oceanic mantle geotherm render the melting of subducted carbonated pelites unavoidable in the long term.

The high concentration of alkalis in carbonated pelitic or psammitic sediments results in alkali-rich calcic to dolomitic carbonatite melts. At the solidus, carbonates melt out and disappear from the residue within a temperature interval ≤ 50–100 °C while melts stay carbonatitic to temperatures of ≥ 400 °C above the solidus (Grassi and Schmidt, 2011a). Compared to silicate melts, carbonate melts have much lower viscosities and better wetting properties (Green and Wallace, 1988). Thus, they are extremely mobile (Hammouda and Laporte, 2000), infiltrate the mantle, and may percolate over long distances. Their particular physical characteristics allow carbonate melts to transport their distinct trace element and isotopic signature into extended mantle domains.

* Corresponding author. Institute of Geochemistry and Petrology, Clausiusstrasse 25, ETH, 8092 Zurich, Switzerland.
E-mail address: max.schmidt@erdw.ethz.ch (M.W. Schmidt).

An involvement of subducted material has been recognized in the source region of many oceanic basalts (Hofmann and White, 1982; Weaver, 1991a,b), continental alkaline rocks (Becker and Le Roex, 2006; Gaffney et al., 2007; Murphy et al., 2002; Ulmer and Sweeney, 2002) and some MORB (Rehkamper and Hofmann, 1997). In particular, the extreme isotopic composition and trace element characteristics of pelagic material has been invoked by Chauvel et al. (1992), Eisele et al. (2002) and Weaver (1991a) to explain the singular EMI signature, i.e. low μ, low $^{206}Pb/^{204}Pb$, unradiogenic Nd ($^{143}Nd/^{144}Nd$), slightly radiogenic Sr ($^{87}Sr/^{86}Sr$), and high $^{207}Pb/^{206}Pb$ and $^{208}Pb/^{206}Pb$ combined with high Ba/Nb-, Sr/Nd- and low Ce/Pb-, Nd/Pb-, and Nb/U-ratios. Murphy et al. (2002) have used these characteristics to decipher the origin of the Gaussberg-lamproites, thought to derive from melting of sediments subducted into the transition zone, where they remained isolated for a long time.

Previous experimental studies on trace element partitioning between minerals and carbonate melts were conducted on typical mantle minerals (Blundy and Dalton, 2000; Brey et al., 2008; Dasgupta et al., 2009; Girnis et al., 2006 and Klemme et al., 1995; Sweeney et al., 1995) demonstrating that extraction of only 0.1 wt.% carbonate melt would remove 30–60% of many incompatible trace elements (Dasgupta et al., 2009). Furthermore, experimental studies have shown that carbonate melts from basaltic or sedimentary eclogites may form at ≥3 GPa (Dasgupta et al., 2004; Grassi and Schmidt, 2011b; Thomsen and Schmidt, 2008; Yaxley and Brey, 2004). Eclogitic residues left back by such melting are quite different from typical mantle residues in their mineralogy, mineral composition and phase abundance. Garnets are more calcic than in peridotitic bulk compositions and pyroxenes are omphacitic to jadeitic compared to diopsidic clinopyroxene in mantle assemblages. In peraluminous and alkali-rich sedimentary eclogites, kyanite or corundum keep the majorite component in garnet at a minimum, and the different potassic phases such as phengite, K-feldspar and K-hollandite may host large amounts of LIL elements including Rb, Sr, Ba, K, Pb, La, Ce and Th.

The partitioning of trace elements between sedimentary residues and silicate melts at ≥5 GPa has been investigated by Aizawa et al. (1999), Irifune et al. (1994), and Rapp et al. (2008) supporting a role of sediment derived melts in the genesis of typical EM mantle signatures. Nevertheless, at >5 GPa, carbonate bearing pelites melt at temperatures lower than carbonate free sediments, in particular above 8 GPa, where the destabilization of phengite leaves an almost

dry residuum. A melting study on dry metapelites at 3–5 GPa (Spandler et al., 2010) indicates that the dry pelite solidus locates far above any subduction geotherm rendering their melting only feasible in an upwelling mantle. It is thus a carbonate melt from carbonated pelites that most likely transfers a sedimentary signature into the mantle. For this reason, we experimentally investigate trace element partitioning during carbonated pelite melting, and define partition coefficients between residual garnet, jadeitic cpx, K-hollandite, CAS-phase, FeTi-perovskite and near solidus carbonate melts at 8, 13, and 22 GPa. We then derive solid residue/carbonate melt bulk partition coefficients and quantify the metasomatic effect of alkali-rich carbonatite melts on the mantle and on its isotopic characteristics, in particular with respect to the EM components.

2. Experimental procedure and analytical technique

2.1. Starting material

The starting materials used in this study (Table 1 and Supplementary Table 1) are two carbonated pelites AM and DG2 (Grassi and Schmidt, 2011a; Thomsen and Schmidt, 2008) mixed with their alkali-rich carbonatite melts in order to increase melt abundances in the charge. The hydrous composition AM corresponds to a Fe-rich calcareous clay from the Antilles simplified in the $K_2O–Na_2O–CaO–FeO–MgO–Al_2O_3–SiO_2–H_2O–CO_2$ (KNCFMASH–CO_2) system. The composition DG2 is an anhydrous carbonated pelite in the TiKNCFMASH–CO_2 system. Both are saturated in coesite/stishovite, kyanite/corundum and carbonates and were made of powders of SiO_2, Al_2O_3, TiO_2, MgO, Na_2SiO_3, fayalite, K-feldspar and wollastonite, milled and ground to <5 μm and mixed with Al(OH)$_3$, $CaCO_3$ and $MgCO_3$ to introduce the desired amounts of H_2O and CO_2. The powders were kept in a desiccator under ambient temperature or in a vacuum oven at 110 °C. Carbonate melts were mixed from appropriate amounts of $MgCO_3$, $FeCO_3$, $CaCO_3$, K_2CO_3, Na_2CO_3, TiO_2, SiO_2 and Al_2O_3. The magnesite is a natural one from Oberdorf (Philipp, 1998), siderite has been synthesized at 2000 bar and 350 °C, following the procedure of French (1971). To the carbonate melt compositions, a mix of 36 trace elements (TX7: Li, Rb, Cs, Be, Sr, Ba, B, Sc, Y, La, Ce, Pr, Nd, Sm, Eu, Gd, Tb, Dy, Er, Yb, Lu, Ti, Zr, Hf, Nb, U, Th, Pb, V, Cr, Mn, Co, Ni, Zn, Ga, and Ge) was added resulting in trace element concentrations between 50 and 150 ppm after the final mixing of the carbonate melt with the pelitic composition in 1:1 and 2:1 ratios.

Table 1
Compositions of the bulk sediments and experimental melts.

	[a]DG2	[b]AM	am-S3b	DG2-S1a	am-S4b	DG2-S2a	am-S6a	DG2-S5a	trace4
P [GPa]			8	8	13	13	22	22	22
T [°C]			1100	1350	1220	1350	1500	1500	1500
SiO_2(wt.%)	54.63	47.60	1.13	1.89	0.48	0.22	0.04	0.05	0.06
TiO_2	0.63	–	–	3.35	–	1.81	–	0.56	0.33
Al_2O_3	20.23	22.80	2.66	2.51	1.31	1.18	0.30	0.26	0.21
FeO	4.86	9.20	7.61	6.27	10.96	7.08	7.35	7.32	5.35
MgO	2.92	2.00	3.19	4.80	2.62	5.35	7.02	7.36	6.04
CaO	5.88	6.80	20.74	21.88	25.59	26.36	18.08	15.33	17.46
Na_2O	3.20	2.40	1.18	1.10	4.72	4.71	19.57	22.74	22.67
K_2O	2.21	3.60	22.96	20.62	12.05	9.43	3.37	3.27	2.90
H_2O	–	1.10	n.a.	–	n.a.	–	n.a.	–	–
CO_2[c]	4.50	4.80	n.a.	37.59	n.a.	43.87	n.a.	43.12	44.99
Total	99.07	100.30	59.47	100.00	57.73	100.00	55.72	100.00	100.00
K_2O/Na_2O (wt.%)	0.69	1.50	19.48	18.82	2.55	2.00	0.17	0.14	0.13
X^*_{Ca}	0.43	0.41	0.67	0.65	0.68	0.67	0.54	0.49	0.58
X^*_{Mg}	0.30	0.17	0.14	0.20	0.10	0.19	0.29	0.33	0.28

X^*_{Mg} = molar MgO/(MgO + CaO + FeO); X^*_{Ca} = molar CaO/(MgO + CaO + FeO).
[a] Carbonated medium X_{Mg}-pelite after Grassi and Schmidt (2011a,b).
[b] Carbonated Fe-rich pelites after Thomsen and Schmidt (2008).
[c] CO_2 content of the melts calculated by difference of 100 and the measured analytical total, note that for the AM composition the presence of both H_2O and CO_2 as volatile components does not allow approximation of CO_2 contents by difference.

Table 2
Summary of the experiments.

Run	capsule	P [GPa]	T [°C]	t [h]	assemblage
am-S3b	Au	8	1100	72	Grt, Cpx, Ky, Coe, Melt
DG2-S1a	Au$_{80}$Pd$_{20}$	8	1350	48	Grt, Cpx, Ky, Coe, Melt
am-S4b	Au	13	1220	72	Grt, Cpx, K-holl, Sti, Crn, Carb, Melt
DG2-S2a	Au$_{80}$Pd$_{20}$	13	1350	48	Grt, Cpx, K-holl, Sti, Crn, Melt
DG2-S5a	Au$_{80}$Pd$_{20}$	22	1500	72	Grt, CAS, K-holl, Sti, Crn, Prv, Carb, Melt
am-S6a	Au$_{80}$Pd$_{20}$	22	1500	72	Grt, CAS, K-holl, Sti, Crn, Melt
trace4	Au$_{80}$Pd$_{20}$	22	1500	48	Grt, CAS, K-holl, Sti, Crn, Na-carb, Melt

2.2. Experimental procedure

Experiments (Table 2) at 8 and 13 GPa were conducted in a 600-ton Walker-type rocking multi-anvil (Schmidt and Ulmer, 2004). To improve equilibration and minimize zonation within the charges, the whole multi-anvil apparatus was rotated by 180 °C during the experiments, continuously during the first 30 min and then every 10 min during the remainder of the experiments. For the experiments at 22 GPa, a traditional 1000-ton Walker multi anvil was used. Tungsten carbide cubes with truncation edge lengths of 11, 8, or 3.5 mm in combination with prefabricated MgO-octahedra of 18, 14, or 10 mm edge length and natural pyrophyllite gaskets were employed at 8, 13, and 22 GPa, respectively. For the experiments at 8 and 13 GPa, the procedure has been described by Grassi and Schmidt (2011a). The smaller 10/3.5 assembly is fully described by Stewart et al. (2006). Temperature was controlled using a B-type (Pt$_{94}$Rh$_6$/Pt$_{70}$Rh$_{30}$) thermocouple and no correction for the effect of pressure was applied. Capsules were placed in the center of the furnace, and quenching was done by turning off heating power, followed by pressure unloading of 15–20 h. After the experiment, capsules (Au or Au$_{80}$Pd$_{20}$, depending on temperature, Table 2), were mounted longitudinally in epoxy resin and polished to the center by dry polishing methods to avoid any loss of alkalis from equilibrium carbonates and from the quench of the carbonate melts. During dry polishing, the open capsules were repeatedly impregnated with low viscosity resin to avoid mechanical loss of quench phases from the carbonate melts. After being analyzed the capsules were kept in a desiccator under vacuum.

2.3. Analytical methods

2.3.1. Electron microprobe

All experimental charges were first analyzed with a JEOL JXA8200 electron microprobe at the Institute for Geochemistry and Petrology, ETH-Zürich with 15 kV acceleration voltage, 20 nA beam current for silicate minerals and 5 nA for carbonates and carbonate liquids. Acquisition times were 10 s for Na and K and 20 s for all other elements, measuring Na and K first to avoid diffusional losses. Beam diameters
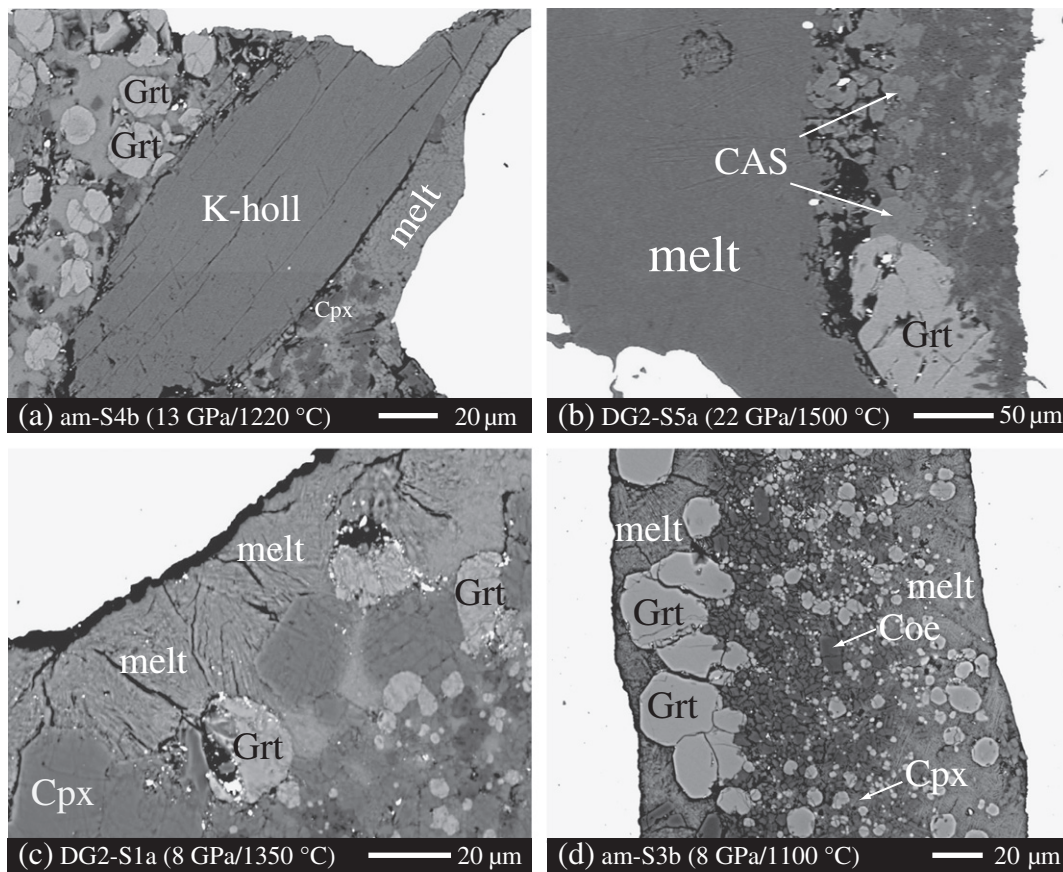

Fig. 1. BSE-images of run products. (a) am-S4b (13 GPa/1220 °C); large K-hollandite crystal coexisting with garnet and small cpx aggregates. (b) DG2-S5a (22 GPa/1500 °C); large garnet crystal in direct contact with Na-rich carbonatite melt and smaller CAS crystals. (c) DG2-S1a (8 GPa/1350 °C); 15–20 μm large cpx crystals of measurable size coexist with garnet and carbonatite melt. (d) am-S3b (8 GPa/1100 °C); garnet coexisting with small aggregates of coesite, kyanite and cpx. Large amounts of melt (ca 40 wt.%) allow for good measurements. Mineral abbreviations: Carb: carbonates (aragonite, magnesite, magnesium calcite and dolomite); Na-carb: Na-rich carbonate; CAS: CaAl$_4$Si$_2$O$_{11}$; Coe: coesite; Cpx: clinopyroxene; Crn: corundum; Grt: garnet; Kfs: potassium feldspar; K-holl: potassium hollandite; Ky: kyanite; Prv: perovskite; Sti: stishovite.

of 1 to 2 μm were used for all silicate and carbonate minerals. Quenched melts, which exhibit beam damage, were analyzed using a defocused beam of 3–20 μm.

2.3.2. Laser ablation-ICP-MS

Trace element analyses were obtained with laser ablation inductively coupled plasma mass spectrometry (LA-ICP-MS) at the Laboratory for Inorganic Chemistry, ETH Zurich. A 193 nm ArF Excimer laser (Gunther et al., 1997) was coupled to an ELAN 6100 DRC ICP-MS. The laser operated at $17 \, J \, cm^{-2}$ using repetition rates between 5 and 10 Hz and crater sizes between 4 and 20 μm for minerals and of 20 μm for quenched melts. Using helium as carrier gas, the laser aerosol produced in a standard cell was transported into the ICP. NIST 610 was used as external reference material. Internal standardization required for element concentration calculations employed major element concentrations (Al and Na) as determined by EPMA (for a detailed description of the technique, see Guillong et al., 2005). The background was acquired for 30 s followed by 15–40 s signal acquisition depending on the pit diameter used during the analysis. The data reduction and concentration calculation is based on the protocol described by Longerich et al. (1996).

3. Results

Phase relations and melting reactions of the dry and H_2O-bearing carbonated pelites used in this study have been defined by Grassi and Schmidt (2011a,b). In these studies, the exact melt composition at near solidus conditions was determined through reverse "sandwich" experiments (Falloon et al., 1997). In this procedure, a thick layer of carbonate melt with the supposed composition derived from measurements of low melt fractions is equilibrated with the carbonated pelite in question (for bulk compositions see Supplementary Table 1). This technique produces relatively large homogeneous areas of melt (Fig. 1) as necessary for analysis using a defocused electron or large laser beam (for EMPA and LA-ICP-MS, respectively). The obtained highly potassic carbonatite melts at 8 and 13 GPa are in equilibrium with garnet, clinopyroxene, coesite/stishovite, kyanite/corundum, K-hollandite (only at 13 GPa), i.e. with a SiO_2 and Al_2O_3 saturated eclogitic assemblage, and in part with carbonate(s) (Table 2). At 22 GPa the highly sodic carbonatite melts coexist with garnet, CAS-phase, stishovite, corundum, K-hollandite, $\pm$ FeTi-perovskite, and $\pm$ magnesite.

3.1. Mineral and melt major element composition

Minerals and melts from the "sandwich" experiments (Table 1 and Supplementary Tables 2–7) have similar compositions as the ones described in Grassi and Schmidt (2011a,b).

Garnet (*grt*) forms subidiomorphic, 10–30 μm large and mostly inclusion-free crystals. Excess Si is low; at 8 GPa garnets have ca. 3.00 Si pfu, at 13 GPa ≤ 3.07 Si pfu, but reach 3.22 Si pfu at 22 GPa. Nevertheless, Si + Ti–Na–K remains below 3 in all experiments, the excess tetravalent cations thus uniquely charge compensate for alkalis but do not indicate a tschermak-type substitution leading to majorite. This lack of *tk*-majorite component results from the coexistence of garnet with kyanite or corundum which yields maximum Al-contents. The most important component at 8 and 13 GPa is grossular with 31–46 mol%. At 22 GPa garnets coexist with the Ca-rich CAS-phase and have lower grossular-contents (9–16 mol%), an increased almandine component of 32 mol% in the AM composition or an increased $NaFe^{3+}$-component of 24 mol% in the DG2 composition. Mg# varies between 25 and 61, increasing with pressure. The DG2 composition yields garnets with higher Mg content than AM due to a higher bulk Mg # (52.4 vs. 27.9, respectively). In spite of the large compositional variability, the measured garnets can be classified as eclogitic. Major differences to eclogitic garnets of basaltic origin are

(i) lower Na-solubilities of 1.5–2.0 wt.% at >16 GPa in our garnets compared to ca. 3 wt.% in basaltic compositions (Okamoto and Maruyama, 2004), (ii) lower Si-contents, garnets from basaltic compositions at 8–18 GPa having typically 3.1–3.30 Si pfu, and (iii) low Mg# compared to 49–75 for garnets from basaltic bulk compositions (Okamoto and Maruyama, 2004; Yasuda et al., 1994).

Clinopyroxenes (*cpx*) form tabular 5–15 μm large grains which were mostly too small to be analyzed by LA-ICP-MS. Trace elements concentrations in cpx could be obtained only from 1 experiment with 57 mol% jadeite component (DG2-S1a). Cpx are extremely sodium- and alumina-rich with a jadeite component of 57–72 mol% at 8 GPa and 80–82 mol% at 13 GPa. The CaTs and Ca-eskolaite components are almost nil and Al(IV) below 0.05 apfu. Compared to eclogitic cpx from basaltic compositions (17–44 mol% at 6–15 GPa) our cpx have much higher jadeite contents and lower Mg# (57–73 in our cpx and 72–81 in basaltic compositions, Dasgupta et al., 2004; Okamoto and Maruyama, 2004; Yasuda et al., 1994).

K-hollandite (*K-holl*) forms elongated prismatic crystals up to 100 μm long and 40 μm wide (am-S4b). At 13 GPa, the Na-hollandite component is small (<4 mol%) but increases to 12 mol% at 22 GPa.

CAS-phase crystallizes only at 22 GPa and contains 1.6–1.7 wt.% K_2O and 0.8–1.0 wt.% Na_2O as well as 1.5–1.7 wt.% TiO_2. Crystal sizes vary between 10 and 30 μm.

FeTi-perovskite crystallizes only at 22 GPa in the Ti-bearing DG2 composition. The stability of this perovskite at slightly lower pressures than in mantle or MORB bulk compositions results from its high-Ti character $(Ti/(Ti+Si)=0.84)$ in combination with a low bulk X_{Mg} of 0.51. Normalization to 2 cations and 6 charges results in a Fe^{3+}/Fe^{tot} of 0.277.

Carbonates coexisting with carbonate melt have a large compositional variability ranging from pure aragonite to Ca-poor and Fe-rich magnesite. As carbonates melt out closely to the solidus, they will not be considered further in this study.

Melts are alkali-rich Ca-carbonatites. The melts quench to mixtures of various carbonate and silicate phases with feathery quench crystals of typically 1–3 μm across and 5–50 μm length. K_2O/Na_2O wt-ratios decrease with increasing pressure from ~20, with 20.6–22.9 wt.% K_2O and ~1 wt.% Na_2O at 8 GPa to values of $K_2O/Na_2O = 0.13$ with 19.6–22.8 wt.% Na_2O and ~3 wt.% K_2O at 22 GPa. Si_2O and Al_2O_3 contents are always below 1.9 and 2.7 wt.%, respectively, TiO_2 varies between 0.3 and 3.4 wt.% (for the DG2 bulk) depending on the coexisting phases and pressure. X^*_{Ca}- (0.49–0.71) and X^*_{Mg}- values (0.10–0.33) are similar to the ones found for melts generated from carbonated basaltic eclogites, which yield X^*_{Ca}'s of 0.44–0.75 and X^*_{Mg}'s of 0.11–0.43 (Dasgupta et al., 2004, 2005; Yaxley and Brey, 2004). These values are clearly different from peridotite derived carbonate melts, which have low X^*_{Ca}'s of 0.12–0–36 and higher X^*_{Mg}'s of 0.53–0.81 (Brey et al., 2008; Dasgupta and Hirschmann, 2007; Ghosh et al., 2009).

3.2. Mineral/melt partition coefficients

Trace element concentrations in the analyzed garnet, clinopyroxene, K-hollandite, CAS-phase, FeTi-perovskite and melts are given in Supplementary Tables 8 and 9. Resulting partitioning coefficients are shown in Fig. 2 and Table 3 (details in Supplementary Table 10). The quenched heterogeneous nature of the melts resulted in an average 1σ standard deviation of trace element concentrations in the melt of 13%. More limiting was the size of the crystals which lead to an average 1σ standard deviation of trace element concentrations of 23%. Nevertheless, the relatively large errors are mostly for elements with low mineral/melt partition coefficients and do not significantly influence the calculated melt compositions.
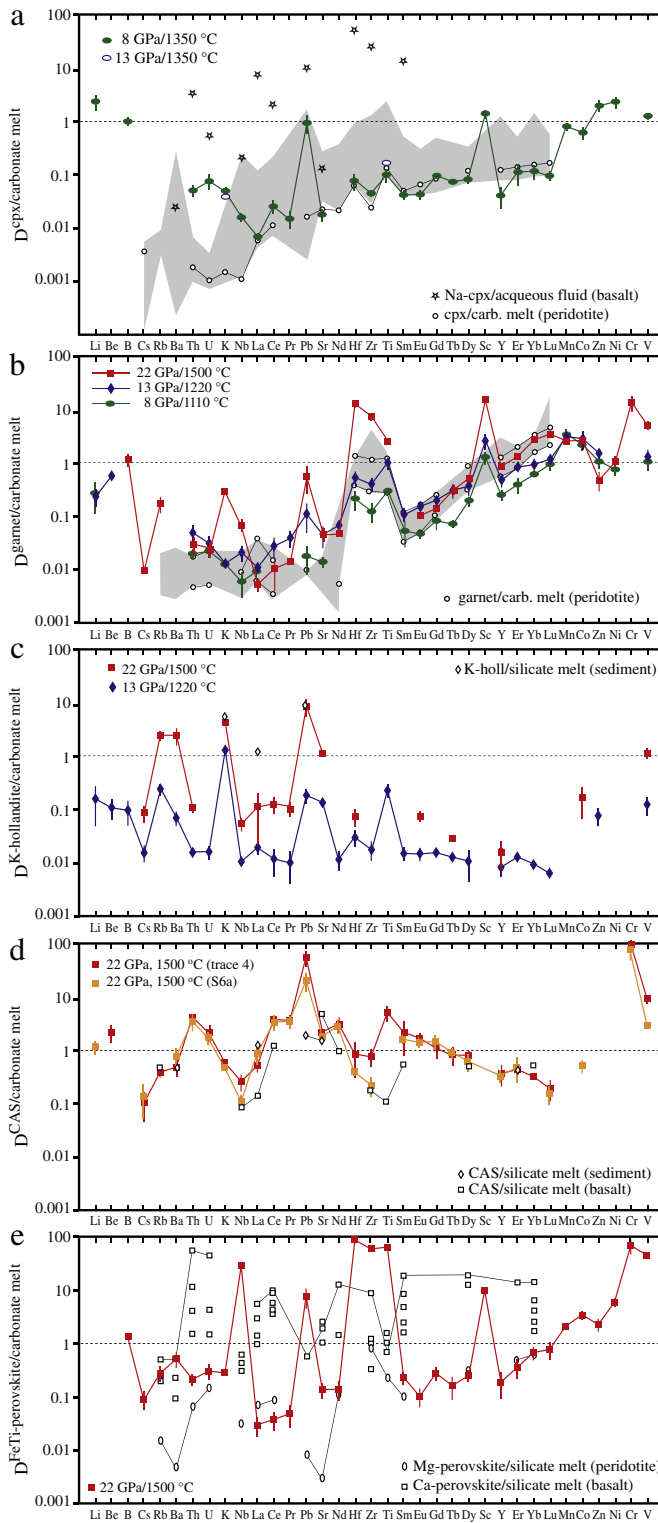
Fig. 2. Element partition coefficients between (a) cpx, (b) garnet, (c) K-hollandite, (d) CAS-phase and (e) FeTi-perovskite and alkali-rich carbonate melt obtained in this study and color coded for pressure. (a) Data constituting the shaded area are from Adam and Green (2001), Blundy and Dalton (2000), Klemme et al. (1995), and Sweeney et al. (1995). Open circles: Dasgupta et al. (2009, in a and b). Stars: Green and Adam (2003). (b) Data constituting the shaded area are from Brey et al. (2008), Green et al. (1992), Sweeney et al. (1992) and Sweeney et al. (1995). (c) Open diamonds: Irifune et al. (1994). (d) and (e): Open squares: Hirose et al. (2004) and for Ca-perovskite also Corgne and Wood (2002), open diamonds: Irifune et al. (1994), open ovals: Corgne and Wood (2002) and Kato et al. (1996).

3.2.1. Clinopyroxene/carbonate melt

The partitioning of trace elements between cpx and the alkali-rich Ca-carbonatite melts (Fig. 2a) could only be measured in one experiment at 8 GPa (DG2-S1a) due to generally small cpx grain sizes in the other experiments. Only Li, B, Na, Sc, V, Ni, and Zn are compatible and Pb, Mn, and Co slightly incompatible, the reminder of the measured elements have $D^{cpx/carb.\ melt} < 0.12$. $D^{cpx/carb.\ melt}$ values for REE, Hf and Sr of this study are comparable to those of Dasgupta et al. (2009) for a peridotite–carbonatite system (Fig. 2a). Nevertheless, $D^{cpx/carb.\ melt}$ values for LILE and Nb are distinctly higher in our system most likely due to the more jadeitic character of our cpx, allowing for larger amounts of large ions on the larger Na-hosting M2-site. Compared to cpx/silicate melt (Adam and Green, 2001; Blundy and Dalton, 2000; Klemme et al., 1995; Sweeney et al., 1995), most elements are generally more incompatible in cpx in equilibrium with carbonate melts, while for cpx/aqueous fluid (Green and Adam, 2003) most elements are less compatible.

As has been discussed before (Grassi and Schmidt, 2011a), Na is highly compatible in cpx at 8 GPa with $D_{Na}^{cpx/carb.melt} \sim 10$ at 8 GPa, decreasing to ~2.5 at 13 GPa. This compatibility is crucial in that the carbonate melts at 8–13 GPa are ultrapotassic with K_2O/Na_2O-ratios of ~20 and ~2 at 8 and 13 GPa, respectively.

3.2.2. Garnet/carbonate melt

Garnet/carbonatite melt partition coefficients from the different pressures are plotted in Fig. 2b and compared to experiments on garnet/silicate melt (Brey et al., 2008; Green et al., 1992; Sweeney et al., 1992; Sweeney et al., 1995) and on garnet/carbonate melt (Dasgupta et al., 2009). In agreement with previous studies, partition coefficients of REE show a steady increase from highly incompatible La ($D_{La} = 0.005$ at 8 GPa) to slightly compatible Lu ($D_{Lu} = 0.87–3.5$ at 8 to 22 GPa). Similar to what was deduced by Dasgupta et al. (2009) from data at 6.6–8.6 GPa, the compatibility of HFSE including Zr, Hf and Ti increases with pressure, from fairly incompatible at 8 GPa to moderately compatible at 13 and highly compatible at 22 GPa. At 8 GPa $D_{Ti} > D_{Hf} > D_{Zr}$ but this changes to $D_{Hf} > D_{Zr} > D_{Ti}$ at 22 GPa. D_{Pb} in our garnet at 8 GPa is 0.018 and comparable to the 0.006–0.02 at 6.6–8.6 GPa measured by Dasgupta et al. (2009) but becomes much higher with pressure, increasing to 0.56 at 22 GPa.

3.2.3. K-hollandite/carbonate melt

At 13 GPa, all measured partition coefficients $D^{K-holl/carb.\ melt}$ except for K are <0.25 (Fig. 2c), thus residual K-hollandite is not expected to leave a strong signature at this pressure (excluding potassium). D's for REE are 0.019 to 0.006 for D_{La} to D_{Lu}. HFSE and LILEs have somewhat higher partition coefficients with D_{Ti} and D_{Rb} of ~0.2 and D_{Li}, D_{Be}, D_B, D_V and D_{Sr} around 0.1 and a D_{Sr}/D_{Nd} ratio of about 11. With increasing pressure the compatibility of potassium in K-holl increases from $D_K = 1.3$ to 4.2 (Grassi and Schmidt, 2011b). A similar behavior is observed for almost all other elements measured at 22 GPa including V, Rb, Sr, Ba, and Pb which become compatible with partition coefficients of 1.1–8.5 at 22 GPa. Irifune et al. (1994) determined partition coefficients for La, Pb and Sr between K-hollandite and silicate melt at P>16 GPa which are much higher than those of K-hollandite and carbonate melt, but which show similar D_{Pb}/D_{Sr} and D_{La}/D_{Pb} ratios. At 8 GPa, no potassium phase is stable above the solidus, which may lead to ultrapotassic carbonate melts with K_2O/Na_2O wt.% ratios of up to ~40. The increasing compatibility of K in K-hollandite with pressure in combination with the disappearance of cpx at $P \geq 16$ GPa and the incompatibility of Na in garnet results in sodic carbonatite melts (Grassi and Schmidt, 2011b) with K_2O/Na_2O wt.% ratios of ~0.15 at 22 GPa.

3.2.4. CAS/carbonate melt

Among all phases measured in this study, the CAS-phase has the most compatible trace elements. Partition coefficients between the

Table 3
Average mineral/melt partitioning coefficients.

P [GPa]	8	8	13	13	22	8	13	22	22	22	22
T [°C]	1100	1350	1220	1350	1500	1350	1220	1500	1500	1500	1500
Mineral	Grt	Grt	Grt	Grt	Grt	Cpx	K-holl	K-holl	CAS-S6a	CAS-t4	FeTi-pvsk
Li	0.28(16)[a]		0.23(8)			2.4(8)	0.16(11)		1.15(32)		
Be		0.57(11)	4.4(11)				0.109(45)			2.2(8)	
B					1.15(28)	1.01(18)	0.098(48)				1.34(18)
Na[b]	0.21(2)	0.34(3)	0.14(2)	0.21(2)	0.088(8)	7.1(3)	0.073(10)	0.066(8)	0.041(4)	0.041(5)	0.042(7)
K[b]	0.013(2)	0.006(1)	0.013(3)	0.029(3)	0.29(3)	0.050(7)	1.28(12)	4.20(22)	0.46(10)	0.58(6)	0.28(4)
Sc	1.29(34)	1.89(44)	2.6(9)	3.5(6)	15.1(13)	1.41(27)					9.9(1.7)
Ti[b]	0.298(47)	0.234(31)	1.01(24)	0.938(24)	2.57(31)	0.101(28)	0.23(6)			5.1(15)	65(9)
V	1.06(35)	1.35(26)	1.32(45)	3.2(7)	4.9(8)	1.26(18)	0.124(48)	1.13(25)	2.87(28)	9.1(16)	45.8(31)
Cr					13.6(43)				74(26)	95(20)	69(22)
Mn	3.4(8)	3.29(38)	3.1(6)	2.56(53)	2.58(13)	0.82(12)					2.12(27)
Co	2.18(44)	2.52(27)	2.8(11)	1.13(28)	2.64(20)	0.62(16)		0.17(10)	0.51(15)		3.5(6)
Ni	0.76(20)	1.45(26)			1.06(26)	2.3(6)					6.0(10)
Zn	1.07(27)	1.60(47)	1.50(36)	2.78(54)	0.48(19)	1.97(48)	0.077(28)				2.3(6)
Ga	1.8(10)	3.5(12)	6.2(20)	3.7(10)	14.5(29)	4.4(13)	0.91(21)	6.4(16)	61(18)	43(9)	30.4(54)
Ge	8.4(33)			29(11)	22(6)				68(22)		67(15)
Rb					0.173(56)		0.24(6)	2.38(45)		0.38(7)	0.27(9)
Sr	0.014(3)		0.045(20)	0.030(19)	0.046(13)	0.018(5)	0.135(25)	1.12(16)	1.83(23)	2.20(23)	0.138(46)
Y	0.252(54)	0.240(45)	0.47(13)	0.58(14)	0.86(11)	0.041(18)	0.009(3)	0.016(8)	0.32(9)	0.36(16)	0.19(10)
Zr	0.123(49)	0.101(24)	0.40(12)	0.60(23)	7.5(12)	0.045(6)	0.018(7)		0.22(9)	0.76(27)	59(6)
Nb	0.006(3)	0.005(1)	0.021(7)	0.14(6)	0.066(20)	0.016(3)	0.011(3)	0.054(15)	0.109(28)	0.26(9)	28.5(39)
Cs					0.010(1)		0.016(6)	0.088(31)	0.14(9)	0.10(6)	0.089(33)
Ba							0.070(23)	2.4(9)	0.76(31)	0.48(16)	0.52(17)
La	0.009(1)	0.010(2)	0.011(2)		0.005(1)	0.007(1)	0.019(5)	0.011(9)	0.87(31)	0.52(14)	0.030(12)
Ce			0.028(12)		0.010(6)	0.026(7)	0.012(6)	0.126(41)	3.3(10)	3.73(49)	0.037(14)
Pr		0.013(2)	0.039(14)		0.014(1)	0.015(5)	0.010(6)	0.102(31)	3.4(9)	3.6(8)	0.048(22)
Nd			0.068(18)		0.047(3)		0.012(5)		2.8(8)	3.1(10)	0.14(6)
Sm	0.053(27)	0.136(38)	0.108(31)			0.042(9)	0.015(4)		1.63(33)	2.1(14)	0.23(6)
Eu	0.046(8)	0.105(23)	0.154(42)	0.086(30)	0.104(9)	0.043(9)	0.015(4)	0.075(17)	1.40(31)	1.68(36)	0.103(41)
Gd	0.083(28)	0.164(23)	0.200(52)	0.203(52)	0.142(21)	0.096(12)	0.016(3)		1.45(43)	1.08(38)	0.28(8)
Tb	0.072(12)	0.118(23)	0.31(10)	0.26(7)	0.31(6)	0.074(9)	0.013(3)	0.029(2)	0.90(21)	0.81(30)	0.16(8)
Dy	0.197(46)	0.118(26)	0.37(14)		0.52(8)	0.082(14)	0.011(6)		0.62(22)	0.79(13)	0.25(6)
Er	0.39(13)	0.42(9)	0.84(15)	1.32(24)	1.32(15)	0.113(50)	0.013(2)		0.49(25)	0.43(7)	0.36(14)
Yb	0.61(7)	0.92(23)	0.93(26)	2.01(45)	2.74(31)	0.117(36)	0.010(2)			0.316(51)	0.67(19)
Lu	0.96(24)	0.87(14)	1.18(24)	1.29(26)	3.45(44)	0.095(17)	0.006(1)		0.15(6)	0.19(8)	0.77(28)
Hf	0.22(9)	0.118(20)	0.53(16)	1.18(29)	12.7(19)	0.076(25)	0.031(11)	0.073(26)	0.39(7)	0.84(53)	88(14)
Pb	0.018(10)		0.11(6)		0.56(30)	0.95(37)	0.184(53)	8.5(29)	20(8)	56(18)	7.8(32)
Th	0.020(5)	0.035(7)	0.049(19)		0.030(11)	0.051(12)	0.016(4)	0.107(20)	3.5(12)	4.14(41)	0.212(51)
U	0.023(6)	0.052(15)	0.031(11)		0.024(8)	0.076(24)	0.016(4)		1.72(50)	2.1(7)	0.30(10)
Zr/Hf	0.57	0.86	0.77	0.50	0.59	0.59	0.58			0.90	0.68
U/Pb	1.3		0.28		0.04	0.08	0.09	0.01	0.09	0.04	0.04
U/Th	1.2		0.63		0.81	1.5	1.0	1.0	0.50	0.52	1.4
Th/La	2.1	3.6	4.5		5.7	7.3	0.83	0.95	4.0	8.0	7.1

[a] Uncertainties are one standard deviation with respect to the mean.
[b] From EMP analysis.

CAS-phase and carbonate melt are 20–56 for Pb, 74–95 for Cr, and between 2 and 9 for Be, Ti, V, Sr, Ce, Pr, Nd, Sm, Th and U (Fig. 2d). Partition coefficients show a steady decrease for the REEs from $D_{Ce} = 3.55$ to $D_{Lu} = 0.198$. The low D_{Nb} (0.11–0.26) leads to high D_{Pb}/D_{Nb} ratios. Our partition coefficients are similar, albeit slightly higher than previous data by Hirose et al. (2004) and Irifune et al. (1994) for silicate melts. The high compatibility of Pb, U and Th and also Sr, Nd and Sm in the CAS-phase leads to a strong fractionation of these elements during partial melting, resulting melts having higher U/Pb-, lower Th/U-, higher Sm/Nd- and higher Rb/Sr-ratios than the source rock. Such a melt eventually evolves to extremely radiogenic Pb compositions.

3.2.5. Fe(Ti)-perovskite/carbonatite melt

Partition coefficients between FeTi-perovskite and carbonatite melt (Fig. 2e) show strongly compatible HFSE including Hf, Zr, Nb, and also V and Cr with $D^{FeTi-perovskite/carb.melt}$ of 28 to 88, analogous to Ti-rich phases such as rutile and sphene. REE are incompatible with partition coefficients increasing from $D_{La} = 0.03$ to $D_{Lu} = 0.77$. Our data for REE partitioning are comparable to those from Hirose et al. (2004) for Mg-perovskite/silicate melt (Fig. 2e). The 2–3 orders of magnitude higher partition coefficients of HFSE for FeTi-perovskite than for MgSi-perovskite can be attributed to the Ti-enrichment and to the carbonatitic character of our melt, the latter in general accommodating limited amounts of high valence cations.

3.3. Lattice strain modeling

Measured partition coefficients have been employed to fit lattice strain parabola (Blundy and Wood, 1994) to mono-, di-, tri-, and in case of perovskite tetra-valent cations in each mineral. The purpose of this modeling is to check for internal consistency of the partition coefficients and to calculate partition coefficients that could not be determined directly but which are needed for the trace element and isotope models. Details of the fits and their results including apparent Young's moduli E, the ideal site-radii r_0 and the partition coefficient D_0 for a cation of size r_0 are given in the electronic appendix. The most remarkable results are:

3.3.1. Garnet

Lattice strain parameters of the 8 GPa-1100 °C garnet which has the lowest alkali-content and Si<3.0 apfu (3-valent cations on the X-site: E = 460 GPa, $r_0 = 0.913$) fit well with predictions from Van Westrenen and Draper (2007). All other garnets have lower r_0 of 0.848–0.899, in part lower apparent Young's moduli for 3-valent cations in the X-site, and a D_0 increasing from 1.6 at 8 GPa to 15.6 at 22 GPa. The lower r_0 renders REE-patterns steeper while at the same time HREE become more and more compatible with pressure.

3.3.2. Cpx

The jadeite-rich character (57 mol% jadeite) results in a large M2-site shifting the r_0 of the 3-valent cation lattice strain parabola in this site to a higher value (1.01 Å) than found by Dasgupta et al. (2009) for cpx with 7–9 mol% jadeite ($r_0 = 0.89$–0.95 Å) or predicted for cpx/silicate melt partitioning (Wood and Blundy, 1997). Nevertheless, this remains inconsequential for the bulk trace element partitioning, as the REE remain largely incompatible in cpx.

3.3.3. K-hollandite

The lattice strain parabola of the mono-valent cations in the VIII-coordinated K site (Zhang et al., 1993) yields a large r_0 of 1.44–1.49. Consequently, the r_0 of the lattice strain parabola of the two-valent cations in this site (1.32–1.38 Å) lies in between the radii of Sr and Ba rendering these (and Pb) relatively compatible in the K-hollandite structure. All three parabolas yield a dramatic increase of D_0 with pressure, by a factor of 2.8 for the alkalis, and by factors of 15 and 8 for the di- and three-valent cations on this site.

3.3.4. CAS phase

Interestingly, the r_0 of the dodecahedral Ca-site (Gautron et al., 1999) of 1.47-1.49 lies just above the ionic radius of Sr but not close to Ca. The REE + Y except of La fit well onto one lattice strain parabola with an apex at a D_0 of 3.6–3.7 and a r_0 close to the ionic radius of Ce leading to a strong depletion of LREE with respect to HREE in the melt. The reasons for the measured D-value of La being 4–7 times lower than the one that would fit the lattice strain parabola remains unknown.

3.3.5. 4-Valent cations

In principal, a lattice strain parabola could be fit to D_{Ti}–D_{Hf}–D_{Zr} in all of the above minerals. Nevertheless, the ionic radii of Hf and Zr are too close and D_{Zr} and D_{Hf} too similar to reliably fit three lattice strain parameters. Suffice to say that D_{Hf} is always larger than D_{Zr} for all minerals ($D_{Hf}/D_{Zr} = 0.49$ to 0.90) and that for the above minerals D_{Th} would not fit onto one lattice strain parabola with D_{Ti}–D_{Hf}–D_{Zr} indicating that Th partitions into a larger size than Ti–Hf–Zr.

3.3.6. FeTi-perovskite

A single lattice strain parabola can be fit to the REE + Y, excluding Sc. This suggests that REE would be hosted on the larger VIII-coordinated site while Sc partitions into the smaller octahedral site (see also Hirose et al., 2004). A single lattice strain parabola with an apex at $D_0 = 98$ and $r_0 = 0.604$ would fit the partition coefficients of the tetra-valent cations. However, Th is likely to partition into the VIII-coordinated site (Corgne and Wood, 2005) while Si, Ge, and Ti should occupy the smaller octahedral site. There is a general problem with site-attributions for cations (Corgne et al., 2005) in particular for those with ionic radii between that of Ti and Fe in this unusual Fe–Ti perovskite. The high partition coefficients for the alkalis, Sr, Pb, and Ba suggest that these would not be accommodated in the same environment as the Fe^{2+} cation dominant on the VIII-coordinated site.

3.4. Bulk partition coefficients for high pressure pelitic residues in equilibrium with carbonate melts

For each pressure, bulk partition coefficients were calculated using average mineral/melt partition coefficients in combination with mineral modes from Grassi and Schmidt (2011a,b) at near-solidus conditions (Table 4 and Fig. 3). The measured partition coefficients are supplemented by partition coefficients calculated from lattice strain modeling or from closest proxy elements (Supplementary Table 10). Despite repeated experiments (not reported here), we did not succeed to crystallize all minerals at all pressures large enough for measurement by LA-ICP-MS. Thus, cpx/carbonate melt partition coefficients at 8 GPa were also employed at 13 GPa. Residual carbonate was not considered as the melt fraction increases rapidly at the solidus until carbonates are melted out. For almost all elements which had partition coefficients calculated, these would increase bulk

Table 4
Bulk partition coefficients and mineral modes.

P[GPa]	8	13	22	22 − pvsk
Li	0.71(20)	0.46(12)		
Be		0.57(11)	0.26(10)	
Na	1.91(25)	0.44(16)	0.048(8)	0.046(8)
K	0.017(2)	0.252(48)	1.24(12)	1.24(12)
Sc	0.77(12)	0.96(25)	4.38(39)	4.37(35)
Ti	0.119(16)	0.36(7)	1.50(20)	5.2(5)
V	0.66(12)	0.60(13)	2.82(31)	5.27(33)
Cr			≥15.4	≥18.0
Mn	1.26(26)	1.04(17)	0.75(4)	0.77(4)
Co	0.84(14)	0.93(31)	0.87(6)	0.97(7)
Ni	0.84(17)	0.47(9)	0.36(8)	0.68(9)
Zn	0.84(15)	0.75(13)	0.24(6)	0.35(6)
Rb	0.0006(3)	0.047(11)	0.72(12)	0.72(12)
Sr	0.009(2)	0.041(8)	0.569(49)	0.553(48)
Y	0.089(17)	0.145(37)	0.296(38)	0.270(34)
Zr	0.050(15)	0.127(34)	2.27(35)	5.52(48)
Nb	0.006(1)	0.011(2)	0.064(13)	1.77(23)
Cs	<0.00001	0.003(1)	0.038(11)	0.042(11)
Ba	<0.00001	0.013(4)	0.69(22)	0.72(23)
La	0.0012(6)	0.0043(21)	0.47(23)	0.43(21)
Ce	0.007(2)	0.014(4)	0.48(6)	0.45(6)
Pr	0.004(1)	0.016(4)	0.46(9)	0.43(8)
Nd	0.006(3)	0.024(5)	0.42(12)	0.39(11)
Sm	0.027(9)	0.040(9)	0.28(17)	0.27(15)
Eu	0.026(3)	0.054(12)	0.251(43)	0.236(40)
Gd	0.051(9)	0.075(15)	0.183(46)	0.183(43)
Tb	0.042(4)	0.103(28)	0.195(40)	0.184(37)
Dy	0.082(15)	0.122(41)	0.251(27)	0.238(24)
Er	0.151(41)	0.263(45)	0.438(45)	0.402(40)
Yb	0.220(23)	0.29(8)	0.83(9)	0.76(8)
Lu	0.32(7)	0.36(7)	1.02(13)	0.93(11)
Hf	0.086(28)	0.170(47)	3.8(5)	8.6(10)
Pb	0.25(9)	0.21(6)	9.0(23)	8.9(21)
Th	0.019(3)	0.025(6)	0.534(50)	0.504(46)
U	0.027(7)	0.023(5)	0.29(9)	0.29(8)
D(Zr/Hf)	0.58	0.75	0.60	0.65
D(Rb/Sr)	0.07	1.12	1.26	1.31
D(Sm/Nd)	4.95	1.66	0.67	0.69
D(U/Pb)	0.11	0.11	0.03	0.03
D(U/Th)	1.39	0.94	0.55	0.57
D(Th/La)	4.1	3.1	5.7	5.6

Mineral modes (wt.%) after Grassi and Schmidt (2011a,b)

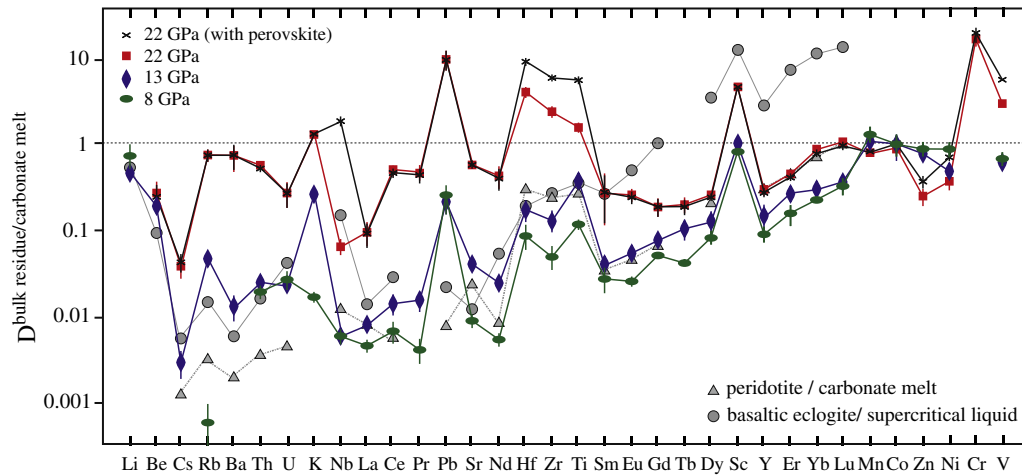|				
Grt	0.31	0.29	0.29	0.25
Cpx	0.26	0.15	–	–
Ky	0.24	0.14	–	–
Cor	–	–	0.10	0.10
Coe/Sti	0.19	0.23	0.22	0.22
K-holl	–	0.19	0.26	0.26
CAS	–	–	0.12	0.11
Prv	–	–	–	0.06

Fig. 3. Solid residue/carbonatite melt bulk partition coefficients calculated from mineral partition coefficients and modal proportions of minerals (Table 4) for Si- and Al-saturated carbonated sediments at 8, 13 and 22 GPa. The data for the garnet lherzolite/carbonate melt system at 6–9 GPa are from Dasgupta et al. (2009), for basaltic eclogite/supercritical liquid in a H_2O-bearing, CO_2-free basalt at 6 GPa from Kessel et al. (2005). Both datasets are directly comparable to our 8 GPa data which have an eclogitic residue.

partition coefficient by <1% and thus do not noticeably influence the calculated melt compositions. The only exceptions are Ti in K-hollandite at 22 GPa, and Co in the CAS phase.

Calculated bulk partition coefficients $D^{bulk\ residue/carb.\ melt}$ (Fig. 3) at 8 and 13 GPa result in generally incompatible LILE and HFSE with partition coefficients mostly between 10^{-1} and 10^{-2} reaching the lowest values for Cs, Rb, Nb and La (Table 4, Fig. 3). For the REE, bulk partition coefficients increase steadily from highly incompatible La to slightly incompatible Lu. Notably high relative $D^{bulk\ residue/carb.\ melt}$ are obtained for Pb, Hf, Zr, Ti and Sc. The transition metals have partition coefficients close to unity. With pressure increasing to 22 GPa, the general compatibility of the LILE, HFSE and LREE increases by more than one order of magnitude; K, Nb (with perovskite), Pb, Hf, Zr, Ti and Sc as well as Cr and V become compatible (Fig. 3). For the HREE this increase is only factors 2–3, leading at 22 GPa to fairly flat REE-patterns. At 22 GPa, a Fe-Ti rich perovskite forms in the residue of the Ti-bearing DG2 sediment composition. From Ti-concentrations and abundances of coexisting minerals, such an FeTi-perovskite can be expected to occur at bulk TiO_2-concentrations >0.5 wt.%. This perovskite increases $D^{bulk\ residue/carb.\ melt}$ 2- to 4-fold for Hf, Zr, and Ti, and 30-fold for Nb. It has thus primarily the effect of sharpening the characteristic subduction signature. The generally high compatibility for some HFSE such as Hf, Zr, and Ti is attributed to a generally low solubility of HFSE in carbonate liquids (Chakhmouradian, 2006; Veksler et al., 1998).

Fig. 3 also compares our bulk partition coefficients to those for lherzolite/carbonatite melt at 8.6 GPa (1265–1470 °C Dasgupta et al., 2009) and of basaltic eclogite/supercritical fluid at 6 GPa (1200 °C, Kessel et al., 2005). With respect to our data at 8 GPa (1100–1350 °C), REE in the lherzolite/carbonate melt system behave similar, but the LILE and Pb are more compatible in the pelite/carbonatite melt system. This difference is mostly due to a higher abundance and the much more sodic character of cpx in the residuum. The pelite/carbonatite melt and the MORB/supercritical liquid systems are, at 8 and 6 GPa, both dominated by garnet + cpx in the residuum. Thus, $D^{bulk\ residue/carb.\ melt}$ for LILE are similar but the RRE patterns much flatter in the pelite/carbonate melt system due to lower garnet fractions.

4. Discussion

The carbonatite melts derived from the subducted sediments are bound to migrate upwards and infiltrate the mantle. An equilibration of the relatively oxidized carbonatite melts ($f_{O2} \geq CCO$) with the much more reducing mantle (typically at or below the iron-wustite buffer at depth >250 km, Frost and McCammon, 2008) leads to redox freezing

of these melts: Carbonate reduces to diamond thus effectively immobilizing the melt (Rohrbach and Schmidt, 2011). As a first order approximation this process can be envisaged as a bulk addition of a carbonatite melt, whose composition is determined by element partitioning with residual phases, without major fractionation in the mantle.

4.1. Carbonate melt metasomatism as a function of pressure

Melt compositions were calculated using the bulk partition coefficients of Table 4 and a simple batch melting equation with 8% partial melting simulating a complete melting out of carbonates (in a sediment containing ~3 wt.% CO_2). Such a choice is justified by the short melting interval of 50–100 °C necessary for carbonates to disappear above the solidus (Grassi and Schmidt, 2011a,b). From the melting reactions defined in these previous studies, carbonate and melt fractions correlate inversely proportional to at least 10–15 wt.% bulk CO_2 at all pressures, above which carbonates would not exhaust first. The initial trace element composition of the sediment is taken from Plank and Langmuir (1998, Antilles Fe-cc clay = AM) and completed for missing elements (Zr, Hf, Nb and Ta) by concentrations from Othman et al. (1989) for pelagic sediments. Furthermore, Kelley et al. (2005) showed that dehydration during subduction leads to a strong fractionation of Pb, U and Th. For this reason we assumed that 65 wt.% of Pb and 25 wt.% of U were lost at sub-arc depths.

As to be expected from the bulk partition coefficients, the most enriched carbonate melt is generated at 8 GPa, the least enriched at 22 GPa (Fig. 4a and Supplementary Table 11). Melt enrichment roughly anti-correlates with the number of residual phases. At 8 GPa the only minerals retaining significant amounts of trace elements are garnet and cpx. At 13 GPa the residue comprises K-hollandite in addition, however, the generally low partition coefficients of K-hollandite at this pressure lead to similar $D^{bulk\ residue/carb.\ melt}$ and thus melt compositions at 8 and 13 GPa. At 22 GPa K-hollandite, CAS-phase, and FeTi-perovskite, combined with the absence of cpx, change the geochemistry of the residue drastically.

The increased negative anomaly of the HFSEs including Hf, Zr and Ti with pressure is mostly caused by an increased compatibility in garnet (Fig. 2b), and is amplified when Fe–Ti-rich perovskite remains residual. Furthermore, the CAS-phase strongly retains Pb, Th and U (in this sequence, Table 3), thus lowering the mobility of these elements yielding a distinctive Pb-isotopic composition after isotopic evolution of these melts.

The characteristic signature of the carbonate melts at 8 GPa with negative Ti and Nb anomalies, high primitive mantle normalized Hf/
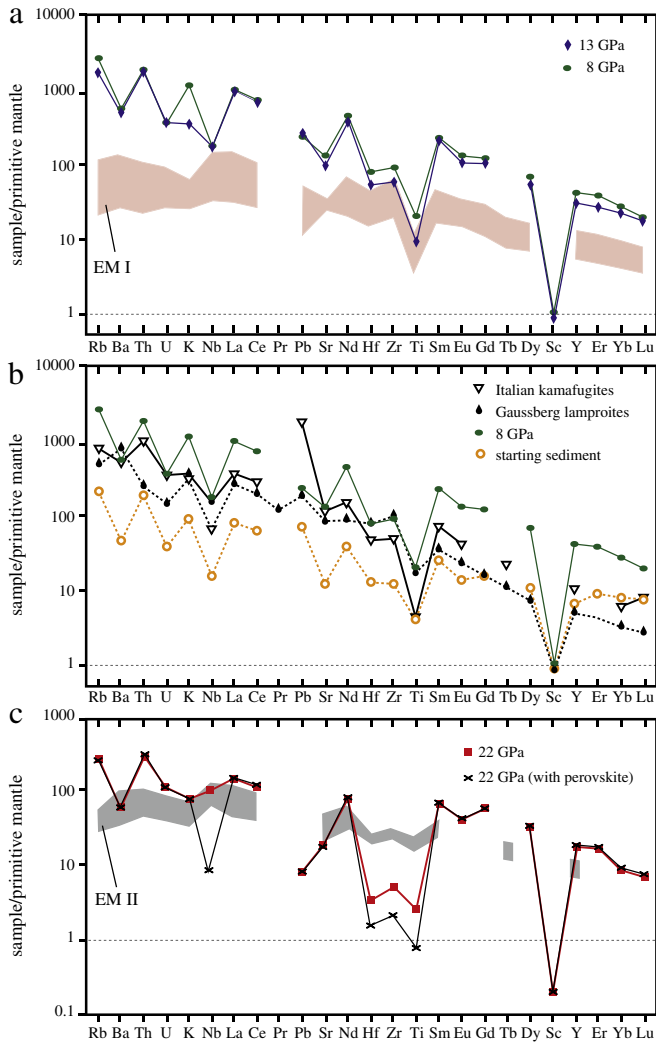
Fig. 4. Calculated trace element patterns for the alkaline carbonatite melts of our Si- and Al-saturated eclogitic carbonated sediments at 8, 13 and 22 GPa. Melt compositions were calculated using the bulk partition coefficients of Table 4 and a simple batch melting equation with 8% melt simulating complete decarbonation (for 3 wt.% bulk CO_2). (a) Comparison between our 8 and 13 GPa melt compositions with the typical EM I OIB patterns (Hofmann, 1997; Lustrino and Dallai, 2003 and Weaver, 1991a). (b) Comparison between the calculated melt at 8 GPa and different ultrapotassic rocks (Gaussberg lamproites after Murphy et al., 2002; Italian kamafugites after Peccerillo, 1998) for which a contamination with continental materials has been postulated. (c) Comparison between the 22 GPa melt and typical EM II pattern in OIB (Weaver, 1991a). The relative negative Hf–Zr–Ti anomaly could be mitigated by larger degrees of melting (see text). All data normalized to primitive mantle (Hofmann, 1988).

Ti- and Th/Nb-ratios, and high K and Pb concentrations match well with many ultrapotassic rocks (Fig. 4b) including lamproites (Mirnejad and Bell, 2006; Murphy et al., 2002), and some Italian kamafugites, shoshonites and leucitites (Avanzinelli et al., 2009; Peccerillo, 2005; Peccerillo et al., 1988). The presence of a sedimentary component in the source regions of these rocks was postulated by many authors (Murphy et al., 2002; Ringwood et al., 1992). Our data corroborate this interpretation and furnish details on the possible nature of the sediment component and a simple mechanism how to transport this sediment signature including potassium and CO_2 into the mantle source region of such alkaline magmas.

The two enriched mantle types EM I and EM II are commonly explained by adding different amounts of oceanic crust including a small sedimentary component (pelagic or terrigenous) to an average mantle composition (Chauvel et al., 1992; Eisele et al., 2002; Hofmann and White, 1982; Weaver, 1991a,b). These enriched mantle reservoirs

are characterized by similar trace element abundances with high LILE/HFSE- and LREE/HFSE-ratios (Weaver, 1991a). Higher Ba contents and related higher Ba/Th and Ba/Nb-ratios distinguish the EM I from the EM II signature, the latter probably originating from a more Ba-depleted sediment type (Weaver, 1991b). Comparing our melts with the EM I and EM II mantle types (Fig. 4a,c) (Hofmann, 1997; Lustrino and Dallai, 2003; Weaver, 1991a), carbonatite melt patterns at 8 and 13 GPa are very similar but significantly more enriched than the EM I signature, making our melts the ideal contaminant yielding a EM I type mantle. On the other hand the melt at 22 GPa with no perovskite in the residuum is more similar to the EM II enriched mantle, although the Hf–Zr–Ti anomaly would need to be mediated (see below).

4.2. Radiogenic isotopes and the mantle end members HIMU, EM I and II

To quantify the metasomatic effect of the sediment derived highly alkaline Ca-carbonate melts on the isotopic composition of the mantle, we calculate the evolution of the different melts derived from a 1.5 Ga old sediment that consists of 94 wt.% pelagic component with an initial $^{87}Sr/^{86}Sr_i$ of 0.7074 (Rehkamper and Hofmann, 1997) and 6 wt.% marine carbonate with an initial $^{87}Sr/^{86}Sr_i$ of 0.706 and a Sr concentration 10 times higher than in the pelagic sediment (Mirota and Veizer, 1994; Plank and Langmuir, 1998). The concentrations of Rb, Nd, Sm, Pb, U and Th in the pelagic component are taken from Rehkamper and Hofmann (1997). Again we assume a dehydration related fractionation of U and Pb during subduction leading to 65 wt.% Pb and 25 wt.% U loss (Kelley et al., 2005). The isotopic evolution (Supplementary Table 11) was calculated assuming zero time between sediment age and melting, yielding an evolution age of 1.5 GPa for the melt reservoirs.

4.2.1. Melting at 8 and 13 GPa and the EM I component

The isotopic evolution of the 8 and 13 GPa melts is characterized by high Rb/Sr and Th/U, and low Sm/Nd ratios. After 1.5 Ga of isotopic evolution in isolation these melts evolve toward compositions with radiogenic $^{87}Sr/^{86}Sr$ (0.7144–0.7155) and unradiogenic $^{143}Nd/^{144}Nd$ (0.5114–0.5115), and with a Pb isotopic composition that is much more radiogenic ($^{207}Pb/^{204}Pb$ ~15.7, $^{208}Pb/^{204}Pb$ ~43, $^{206}Pb/^{204}Pb$ ~19, Supplementary Table 12) than that of depleted mantle types (Fig. 5). When migrating into the mantle, these carbonatite melts yield mixed reservoirs which reproduce the EM I mantle type with <0.1–0.2 wt.% of sediment melt. The high degree of trace element enrichment in the carbonate melts, compared to the unmolten sediment source renders the physically easy-to-achieve migration of these melts into the mantle one order of magnitude more effective than a mechanical bulk mixing-process between sediments and mantle, 0.1 wt.% of melt having the same effect as adding 1–3 wt.% of sediment. An unfractionated bulk mixing of carbonated pelite with mantle at ≥6 GPa (Grassi and Schmidt, 2011b) is not truly an option: assuming that the slab and mantle are both near adiabatic before intimate mixing could occur, the solidus of carbonated sediments would be overstepped by several 100 °C. Thus carbonatite melting and melt migration are unavoidable and the bulk carbonated sediment would not bulk mix with the mantle.

4.2.2. Melting at 22 GPa and the EM II component

Melting at 22 GPa with residual CAS-phase and possibly FeTi-perovskite results in an extreme fractionation within the U–Th–Pb system. This leads to carbonatite melts at 22 GPa that would evolve to extremely radiogenic Pb ($^{207}Pb/^{204}Pb$ ~17.6, $^{208}Pb/^{204}Pb$ ~74, $^{206}Pb/^{204}Pb$ ~40), but less radiogenic $^{87}Sr/^{86}Sr$ (~0.7131) and $^{143}Nd/^{144}Nd$ (~0.5121) than at 8–13 GPa. Mixing of 0.5–1 wt.% of such melts with depleted mantle yields a reservoir which fits well with the EM II Nd- and Sr signature but which is slightly too radiogenic in $^{206}Pb/^{204}Pb$ for EM II. The extremely radiogenic Pb isotopic composition of the 22 GPa carbonatite melt is unknown in melts erupted at the surface.
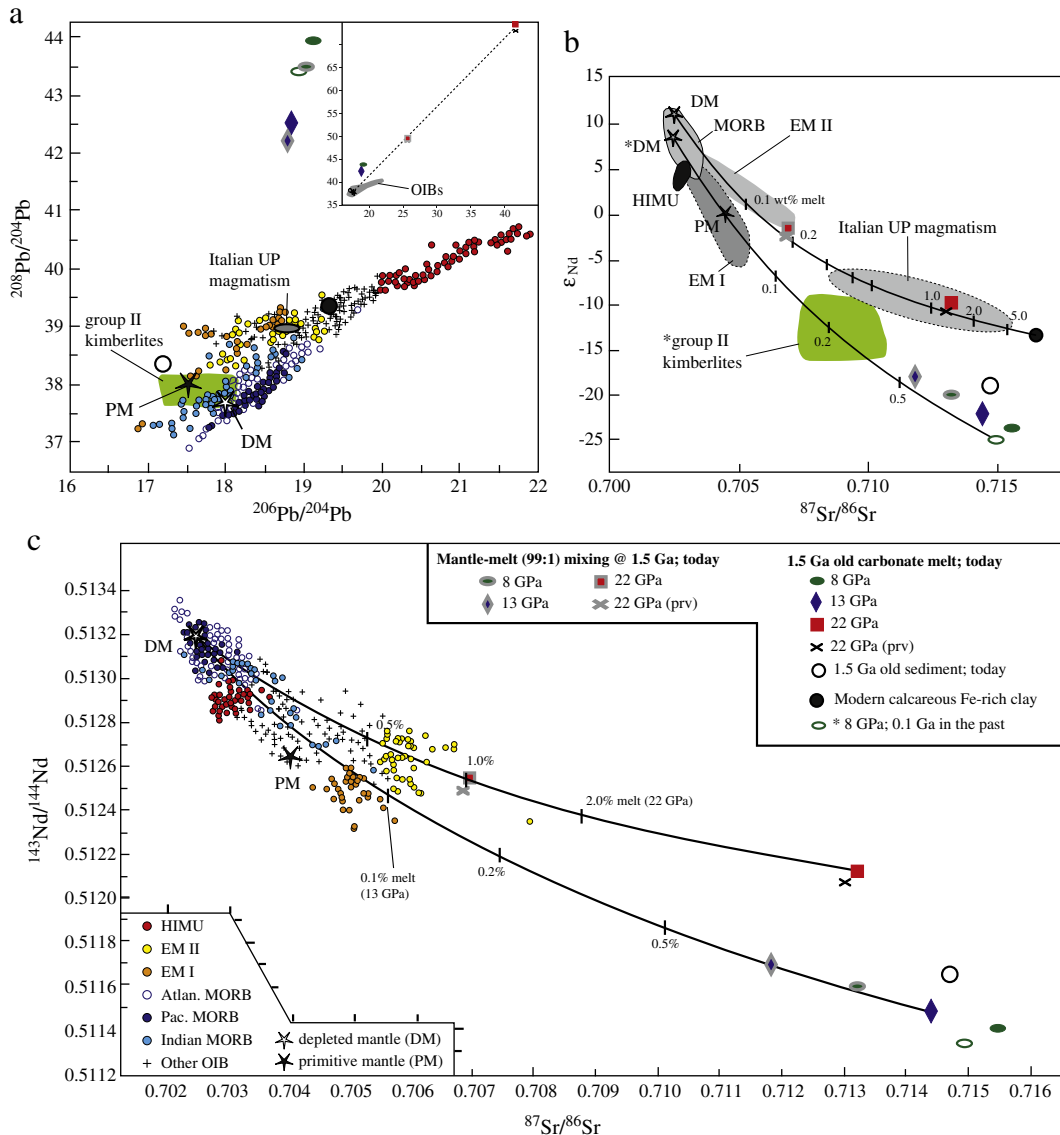
Fig. 5. Sr, Nd and Pb isotopic compositions of sediments and their carbonatite melts at 8, 13 and 22 GPa (F = 0.08) evolved separately or together with the mantle (99% mantle + 1% melt) for 1.5 Ga. Composition of present-day depleted mantle (DM) from Salters and Stracke (2004) and of primitive mantle from Hofmann (1997). Present-day isotope composition for pelagic clays (filled black circle) after Plank and Langmuir (1998). Isotopic compositions of OIB with different EM I, EM II and HIMU flavors and MORB (Hofmann, 1997) are plotted for comparison. (a) Pb isotopic compositions for sediments, carbonatite melts evolving seperately, and mixed reservoirs evolving for 1.5 Ga compared to isotopic compositions of OIBs, today composition of Italian ultrapotassic rocks (Gasperini et al., 2002) and to the initial South African group II kimberlites (Becker and Le Roex, 2006 and Smith, 1983). (b) Sr and Nd isotopic compositions of group II kimberlites lay on the mixing line between 0.1 Ga old depleted mantle and 0.1 Ga old (after 1.4 Ga evolution) *8 GPa melt. The Italian ultrapotassic rocks lay along the mixing line between present-day depleted mantle and pelagic sediments (as for Pb) arguing for mixing with relatively recent sediments. (c) Sr and Nd isotopic compositions for sediments, carbonatite melts and mixed reservoirs evolved for 1.5 Ga compared to isotopic compositions of OIBs. The addition of only minor amounts (<1 wt.%) of the pelite derived carbonatite melts to depleted or primitive mantle yields mantle domains covering a wide compositional spectrum of the EM mantle flavor. For details see text.

4.2.3. Common evolution of a sediment melt + mantle reservoir in metasomatized domains

Realistically, the carbonate melts will migrate into the mantle upon formation and mix with the mantle at the time of its generation. We thus calculated the isotopic evolution of mantle domains metasomatized by carbonate melt (Supplementary Table 11, Fig. 5). Down to 0.1 wt.% carbonate melt, the sedimentary component remains dominant because of their much higher Rb, Sr, Sm, Nd, U, Th, and Pb concentrations compared to any mantle. After an evolution of 1.5 Ga, the resulting isotopic Pb, Sr, and Nd composition of these metasomatized mantle domains does not differ much from mantle:melt-mixing (in corresponding proportions) after a separated and isolated isotopic evolution of the two components. The reason for this is the extreme trace element enrichment (1:500–1:10,000) of the carbonate melt compared to depleted mantle. The carbonatite melt–mantle mixing

models demonstrate that by varying the pressure of melting of carbonated clastic sediments, the sediment composition, the deposition and melting age of the sediment, the devolatilization history before melting, and the time of melt mixing with a mantle source, a broad range of isotopic compositions could be obtained covering the entire range of isotopic EM-type mantle signatures (Figs. 4–6). The mixing models suggest that EM type ocean island basalts would require a source metasomatized by 0.1–1 wt.% carbonate melt.

4.3. Melting of re-enriched depleted mantle

The high degree of incompatible element enrichment in most alkaline magma suites (various OIBs, kimberlites, lamproites and other highly alkaline rocks) implies a metasomatic enrichment of the source region. Such an enrichment in LILE and LREE is often
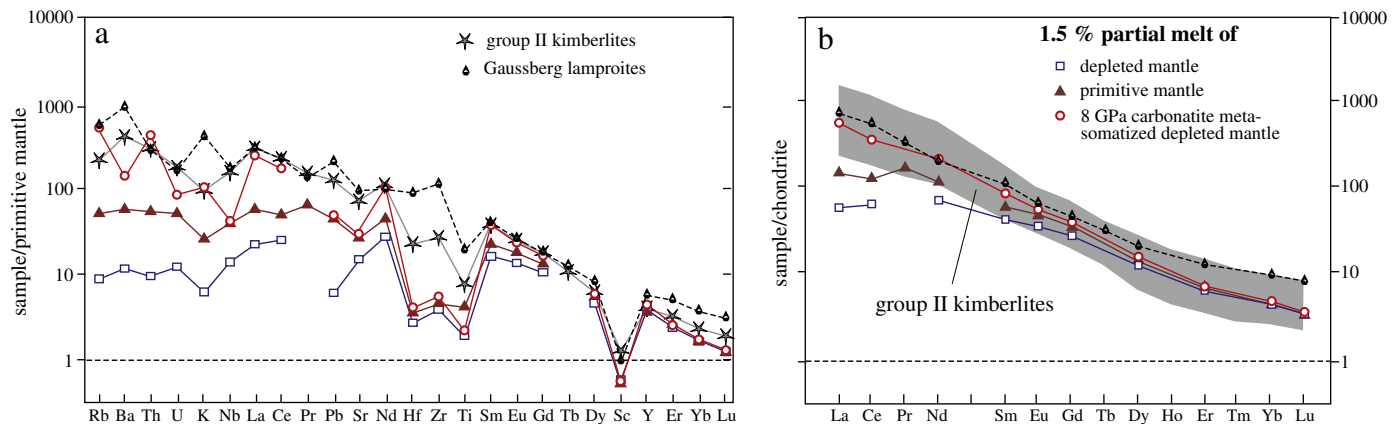
Fig. 6. Calculated trace elements patterns for a melt generated from a depleted mantle (Salters and Stracke, 2004) re-enriched by 0.4 wt.% of our 8 GPa melt composition and using a simple batch melting equation with F = 1.5%. (a) Primitive mantle normalized carbonatite melt compared to South African group II kimberlites (Becker and Le Roex, 2006) and Gaussberg lamproites (Murphy et al., 2002). Differences in HFSE are due to high residue/carbonatite bulk partition coefficients of our melts. Differences in LILE elements are due to our sediment bulk composition which is relatively Ba-depleted (Plank and Langmuir, 1998) and could be mitigated by selecting a different pelagic sediment component (Fig. 5b). (b) Chondrite-normalized (McDonough and Sun, 1995) REE pattern for the same melt compared to group II kimberlites and the Gaussberg lamproites. Melt compositions calculated from a batch melting equation with F = 1.5% melt applied to both a primitive (Hofmann, 1988) and a depleted mantle (Salters and Stracke, 2004).

coupled with evidence for a refractory mantle source with high Mg#, high Ni-concentrations and low Al_2O_3 and HREE suggesting a depletion of the source mantle previous to metasomatic enrichment (Brey et al., 2008).

We thus calculated melt compositions resulting from a depleted mantle (Salters and Stracke, 2004) re-enriched by our K-rich carbonatite melt generated at 8 GPa. For this purpose we employed a batch melting equation and partition coefficients for garnet lherzolite/carbonatite melt at pressures of 6.6–8.6 GPa from Dasgupta et al. (2009). We optimized the re-fertilizing carbonatite melt fraction (0.4 wt.%) and the degree of mantle melting (F = 1.5%) to fit REE-concentrations to group II kimberlites from South Africa (Becker and Le Roex, 2006) and to the Gaussberg lamproites (Murphy et al., 2002). Both show characteristics related to recycling of crustal material through subduction processes (McCandless, 1999; Mirnejad and Bell, 2006; Murphy et al., 2002; Ringwood et al., 1992), and our calculated melts well match the composition of these magma types (Fig. 6). The main difference lies in a greater HFSE-depletion in our calculated melt. This depletion could be mitigated through higher degrees of sediment melting, when melt compositions evolve from carbonatite to more Si-rich melts leading to an incompatibility of HFSE increased by an order of a magnitude for silicate with respect to carbonatite melts (Veksler et al., 1998). Furthermore, the observed small discrepancies concerning some LILE including Rb and Ba could be adjusted by selecting a different initial chemical composition of the clastic sediment component (Plank and Langmuir, 1998), ours being highly depleted in Ba and enriched in Rb and Th.

The isotopic composition of group II kimberlites from South Africa shows highly radiogenic $^{87}Sr/^{86}Sr$ (0.708–0.712) and unradiogenic $^{143}Nd/^{144}Nd$ (εNd between −7 and −17) relative to primitive mantle (Becker and Le Roex, 2006). The South African group II kimberlites erupted between 100 and 150 Ma ago (Becker and Le Roex, 2006). Orogenesis and continental collision within the South African craton, supposedly ending subduction, dates to ca. 1 Ga (Namaqua–Natal belt of the Kibarian orogenic period; Thomas et al., 1994; Hopp et al., 2008; Lazarov et al., 2009) and to ca. 280 Ma (the permo-triassic Cape Fold belt; Frimmel et al., 2001). Fig. 5b illustrates the effect of mixing between a depleted mantle and our 8 GPa melt on the Nd and Sr isotopic compositions. Compositions have been calculated for 100 Ma old reservoirs (after 1.4 Ga evolution for the 8 GPa melt). The mixing of a depleted mantle with 0.3 to 1.5 wt.% of our sediment derived melt fits the initial $^{87}Sr/^{86}Sr$ and εNd composition of group II kimberlites. These data strongly support the hypothesis of a relation

between group II kimberlites and lamproites with carbonatite melt subduction zone metasomatism and the related enrichment of a depleted mantle source region. Our model is able to explain the observed trace elements abundances and isotopic characteristics of these magmas through migration of sediment derived carbonate melts into the sublithospheric depleted mantle.

5. Conclusions

The partition coefficients between typical eclogite and higher pressure minerals and alkali-rich calcic to dolomitic carbonatite melts measured in this study, allow for quantifying the metasomatic effect of such highly enriched sediment derived carbonatite melts on mantle reservoirs from 150 to 660 km depths. In the presence of cpx, calculated trace element characteristics of these melts match well with many ultrapotassic rocks such as kamafugites and lamproites. Addition of 0.1–1 wt.% of these melts to a depleted mantle followed by later remelting of this re-enriched mantle source produces magmas with isotopic characteristics of group II kimberlites. The parent/daughter element fractionation induced by melting of carbonated eclogitic pelites leads to reservoirs having distinct Rb/Sr, U/Pb, Th/U and Sm/Nd ratios and also higher Sr, Nd and Pb concentrations than the unmelted sedimentary source. Trace element characteristics and the isotopic evolution of these melts mixed with the mantle cover the entire compositional range defined by the EM flavors of OIBs, thus lending a face to the sedimentary component in the EM mantle types.

Appendix A. Supplementary data

Supplementary data to this article can be found online at doi:10.1016/j.epsl.2012.01.023.

References

Adam, J., Green, T., 2001. Experimentally determined partition coefficients for minor and trace elements in peridotite minerals and carbonatitic melt, and their relevance to natural carbonatites. Eur. J. Mineral. 13, 815–827.

Aizawa, Y., Tatsumi, Y., Yamada, H., 1999. Element transport by dehydration of subducted sediments: implication for arc and ocean island magmatism. Island Arc 8, 38–46.

Avanzinelli, R., Lustrino, M., Mattei, M., Melluso, L., Conticelli, S., 2009. Potassic and ultrapotassic magmatism in the circum-Tyrrhenian region: significance of carbonated pelitic vs. pelitic sediment recycling at destructive plate margins. Lithos 113, 213–227.

Becker, M., Le Roex, A.P., 2006. Geochemistry of South African on- and off-craton, Group I and Group II kimberlites: petrogenesis and source region evolution. J. Petrol. 47, 673–703.

Blundy, J., Dalton, J., 2000. Experimental comparison of trace element partitioning between clinopyroxene and melt in carbonate and silicate systems, and implications for mantle metasomatism. Contrib. Mineral. Petrol. 139, 356–371.

Blundy, B.J., 1994. Prediction of crystal-melt partitioning coefficients from elastic moduli. Nature 372, 452–454.

Brey, G.P., Bulatov, V.K., Girnis, A.V., Lahaye, Y., 2008. Experimental melting of carbonated peridotite at 610 GPa. J. Petrol. 49, 797–821.

Chakhmouradian, A.R., 2006. High-field-strength elements in carbonatitic rocks: geochemistry, crystal chemistry and significance for constraining the sources of carbonatites. Chem. Geol. 235, 138–160.

Chauvel, C., Hofmann, A.W., Vidal, P., 1992. HIMU EM — the French–Polynesian connection. Earth Planet. Sci. Lett. 110, 99–119.

Corgne, A., Wood, B.J., 2002. CaSiO₃ and CaTiO₃ perovskite-melt partitioning of trace elements: implications for gross mantle differentiation. Geophys. Res. Lett. 29 (19), 1933. doi:10.1029/2001GL014398.

Corgne, A., Wood, B.J., 2005. Trace element partitioning and substitution mechanisms in calcium perovskites. Contrib. Mineral. Petrol. 149, 85–97.

Corgne, A., Liebske, C., Wood, B.J., Rubie, D.C., Frost, D.J., 2005. Silicate perovskite-melt partitioning of trace elements and geochemical signature of a deep perovskite reservoir. Geochim. Cosmochim. Acta 69, 485–496.

Dasgupta, R., Hirschmann, M.M., 2007. A modified iterative sandwich method for determination of near-solidus partial melt compositions. II. Application to determination of near-solidus melt compositions of carbonated peridotite. Contrib. Mineral. Petrol. 154, 647–661.

Dasgupta, R., Hirschmann, M.M., Dellas, N., 2005. The effect of bulk composition on the solidus of carbonated eclogite from partial melting experiments at 3 GPa. Contrib. Mineral. Petrol. 149, 288–305.

Dasgupta, R., Hirschmann, M.M., McDonough, W.F., Spiegelman, M., Withers, A.C., 2009. Trace element partitioning between garnet lherzolite and carbonatite at 6.6 and 8.6 GPa with applications to the geochemistry of the mantle and of mantle-derived melts. Chem. Geol. 262, 57–77.

Dasgupta, R., Hirschmann, M.M., Withers, A.C., 2004. Deep global cycling of carbon constrained by the solidus of anhydrous, carbonated eclogite under upper mantle conditions. Earth Planet. Sci. Lett. 227, 73–85.

Eisele, J., Sharma, M., Galer, S.J.G., Blichert-Toft, J., Devey, C.W., Hofmann, A.W., 2002. The role of sediment recycling in EM-1 inferred from Os, Pb, Hf, Nd, Sr isotope and trace element systematics of the Pitcairn hotspot. Earth Planet. Sci. Lett. 196, 197–212.

Falloon, T.J., Green, D.H., O'Neill, H.S., Hibberson, W.O., 1997. Experimental tests of low degree peridotite partial melt compositions: implications for the nature of anhydrous near-solidus peridotite melts at 1 GPa. Earth Planet. Sci. Lett. 152, 149–162.

French, B.M., 1971. Stability relations of siderite (FeCO₃) in system Fe–C–O. Am. J. Sci. 271, 37–41.

Frimmel, H.E., Folling, P.G., Diamond, R., 2001. Metamorphism of the Permo-Triassic Cape Fold Belt and its basement, South African. Mineral. Petrol. 73, 325–346.

Frost, D.J., McCammon, C.A., 2008. The redox state of the Earth's mantle. Annu. Rev. Earth Planet. Sci. 36, 389–420.

Gaffney, A.M., Blichert-Toft, J., Nelson, B.K., Bizzarro, M., Rosing, M., Albarede, F., 2007. Constraints on source-forming processes of West Greenland kimberlites inferred from Hf-Nd isotope systematics. Geochim. Cosmochim. Acta 71, 2820–2836.

Gasperini, D., Blichert-Toft, J., Bosch, D., Del Moro, A., Macera, P., Albarede, F., 2002. Upwelling of deep mantle material through a plate window: evidence from the geochemistry of Italian basaltic volcanics. J. Geophys. Res. 107, 2367. doi:10.1029/2001JB000418.

Gautron, L., Angel, R.J., Miletich, R., 1999. Structural characterization of the high-pressure phase CaAl₄Si₂O₁₁. Phys. Chem. Mineral. 27, 47–51.

Ghosh, S., Ohtani, E., Litasov, K.D., Terasaki, H., 2009. Solidus of carbonated peridotite from 10 to 20 GPa and origin of magnesiocarbonate melt in the Earth's deep mantle. Chem. Geol. 262, 17–28.

Girnis, A.V., Bulatov, V.K., Lahaye, Y., Brey, G.P., 2006. Partitioning of trace elements between carbonate–silicate melts and mantle minerals: experiment and petrological consequences. Petrology 14, 492–514.

Grassi, D., Schmidt, M.W., 2011a. Melting of carbonated pelites at 8–13 GPa: generating K-rich carbonatites for mantle metasomatism. Contrib. Mineral. Petrol. 162, 169–191.

Grassi, D., Schmidt, M.W., 2011b. The melting of carbonated pelites from 70 to 700 km depth. J. Petrol. 52, 765–789.

Green, D.H., Wallace, M.E., 1988. Mantle metasomatism by ephermal carbonatite melts. Nature 336, 459–462.

Green, T.H., Adam, J., 2003. Experimentally-determined trace element characteristics of aqueous fluid from partially dehydrated mafic oceanic crust at 3.0 GPa, 650–700 degrees C. Eur. J. Mineral. 15, 815–830.

Green, T.H., Adam, J., Sie, S.H., 1992. Trace-element partitioning between silicate minerals and carbonatite at 25 kbar and application to mantle metasomatism. Mineral. Petrol. 46, 179–184.

Guillong, M., Hametner, K., Reusser, E., Wilson, S.A., Gunther, D., 2005. Preliminary characterisation of new glass reference materials (GSA-1G, GSC-1G, GSD-1G and GSE-1G) by laser ablation-inductively coupled plasma-mass spectrometry using 193 nm, 213 nm and 266 nm wavelengths. Geostand. Geoanal. Res. 29, 315–331.

Gunther, D., Frischknecht, R., Heinrich, C.A., Kahlert, H.J., 1997. Capabilities of an Argon Fluoride 193 nm excimer laser for laser ablation inductively coupled plasma mass spectrometry microanalysis of geological materials. J. Anal. Atomic Spectrom. 12, 939–944.

Hammouda, T., Laporte, D., 2000. Ultrafast mantle impregnation by carbonatite melts. Geology 28, 283–285.

Hirose, K., Shimizu, N., van Westrenen, W., Fei, Y.W., 2004. Trace element partitioning in Earth's lower mantle and implications for geochemical consequences of partial melting at the core-mantle boundary. Phys. Earth Planet. Int. 146, 249–260.

Hofmann, A.W., 1988. Chemical differentiation of the earth — the relationship between mantle, continental-crust, and oceanic-crust. Earth Planet. Sci. Lett. 90, 297–314.

Hofmann, A.W., 1997. Mantle geochemistry: the message from oceanic volcanism. Nature 385, 219–229.

Hofmann, A.W., White, W.M., 1982. Mantle plume from ancient oceanic crust. Earth Planet. Sci. Lett. 57, 421–436.

Hopp, J., Trieloff, M., Brey, G.P., Woodland, A.B., Simon, N.S.C., Wijbrans, J.R., Siebel, W., Reitter, E., 2008. Ar-40/Ar-39-ages of phlogopite in mantle xenoliths from South African kimberlites: evidence for metasomatic mantle impregnation during the Kibaran orogenic cycle. Lithos 106, 351–364.

Irifune, T., Ringwood, A.E., Hibberson, W.O., 1994. Subduction of continental-crust and terrigenous and pelagic sediments — an experimental study. Earth Planet. Sci. Lett. 126, 351–368.

Kato, T., Ohtani, E., Ito, Y., Onuma, K., 1996. Element partitioning between silicate perovskites and calcic ultrabasic melt. Phys. Earth Planet. Int. 96, 201–207.

Kelley, K.A., Plank, T., Farr, L., Ludden, J., Staudigel, H., 2005. Subduction cycling of U, Th, and Pb. Earth Planet. Sci. Lett 234, 369–383.

Kessel, R., Schmidt, M.W., Ulmer, P., Pettke, T., 2005. Trace element signature of subduction-zone fluids, melts and supercritical liquids at 120–180 km depth. Nature 437, 724–727.

Klemme, S., Vanderlaan, S.R., Foley, S.F., Gunther, D., 1995. Experimentally determined trace and minor element partitioning between clinopyroxene and carbonatite melt under upper-mantle conditions. Earth Planet. Sci. Lett. 133, 439–448.

Lazarov, M., Brey, G.P., Weyer, S., 2009. Time steps of depletion and enrichment in the Kaapvaal craton as recorded by subcalcic garnets from Finsch (SA). Earth Planet. Sci. Lett. 279, 1–10.

Longerich, H.P., Jackson, S.E., Gunther, D., 1996. Laser ablation inductively coupled plasma mass spectrometric transient signal data acquisition and analyte concentration calculation. J. Anal. Atomic Spectrom. 11, 899–904.

Lustrino, M., Dallai, L., 2003. On the origin of EM-I end-member. Neues Jahrbuch Mineral. Abhandlungen 179, 85–100.

McCandless, T.E., 1999. Kimberlites: mantle expressions of deep-seated subduction. In: Gurney, J.J., Gurney, J.L., Pascoe, M.D., Richardson, S.H. (Eds.), Proceedings of the 7th International Kimberlite Conference, Volume 2. Red Roof Publishers, Cape Town, South Africa, pp. 545–549.

McDonough, W.F., Sun, S.S., 1995. The composition of the earth. Chem. Geol. 120, 223–253.

Mirnejad, H., Bell, K., 2006. Origin and source evolution of the Leucite Hills lamproites: evidence from Sr–Nd–Pb–O isotopic compositions. J. Petrol. 47, 2463–2489.

Mirota, M.D., Veizer, J., 1994. Geochemistry of precambrian carbonates.6. Aphebian albanel formations, Quebec, Canada. Geochim. Cosmochim. Acta 58, 1735–1745.

Murphy, D.T., Collerson, K.D., Kamber, B.S., 2002. Lamproites from Gaussberg, Antarctica: possible transition zone melts of Archaean subducted sediments. J. Petrol. 43, 981–1001.

Okamoto, K., Maruyama, S., 2004. The eclogite–garnetite transformation in the MORB +H₂O system. Phys. Earth Planet. Int. 146, 283–296.

Othman, D.B., White, W.M., Patchett, J., 1989. The geochemistry of marine sediments, island arc magma genesis, and crust-mantle recycling. Earth Planet. Sci. Lett. 94, 1–21.

Peccerillo, A., 1998. Relationships between ultrapotassic and carbonate-rich volcanic rocks in central Italy: petrogenetic and geodynamic implications. Lithos 43, 267–279.

Peccerillo, A., 2005. Plio-Quaternary Volcanism in Italy. Springer-Verlag, Berlin.

Peccerillo, A., Poli, G., Serri, G., 1988. Petrogenesis of orenditic and kamafugitic rocks from central Italy. Can. Mineral. 26, 45–65.

Philipp, R.W., Phasenbeziehungen im System MgO–H₂O–CO₂–NaCl, Ph.D. dissertation, ETH, Zürich, 1998.

Plank, T., Langmuir, C.H., 1998. The chemical composition of subducting sediment and its consequences for the crust and mantle. Chem. Geol. 145, 325–394.

Rapp, R.P., Irifune, T., Shimizu, N., Nishiyama, N., Norman, M.D., Inoue, J., 2008. Subduction recycling of continental sediments and the origin of geochemically enriched reservoirs in the deep mantle. Earth Planet. Sci. Lett. 271, 14–23.

Rehkamper, M., Hofmann, A.W., 1997. Recycled ocean crust and sediment in Indian Ocean MORB. Earth Planet. Sci. Lett. 147, 93–106.

Ringwood, A.E., Kesson, S.E., Hibberson, W., Ware, N., 1992. Origin of kimberlites and related magmas. Earth Planet. Sci. Lett. 113, 521–538.

Rohrbach, A., Schmidt, M.W., 2011. Redox freezing and melting in the Earth's deep mantle resulting from carbon–iron redox coupling. Nature 472, 209–212.

Salters, V.J.M., Stracke, A., 2004. Composition of the depleted mantle. Geochem.Geophys. Geosys. 5, Q05B07. doi:10.1029/2003GC000597.

Schmidt, M.W., Ulmer, P., 2004. A rocking multianvil: elimination of chemical segregation in fluid-saturated high-pressure experiments. Geochim. Cosmochim. Acta 68, 1889–1899.

Smith, C.B., 1983. Pb, Sr and Nd isotopic evidence for sources of southern African cretaceous kimberlites. Nature 304, 51–54.

Spandler, C., Yaxley, G., Green, D.H., Scott, D., 2010. Experimental phase and melting relations of metapelite in the upper mantle: implications for the petrogenesis of intraplate magmas. Contrib. Mineral. Petrol. 160, 569–589.

Stewart, A.J., van Westrenen, W., Schmidt, M.W., Melekhova, E., 2006. Effect of gasketing and assembly design: a novel 10/3.5 mm multi-anvil assembly reaching perovskite pressures. High Press. Res. 26, 293–299.

Sweeney, R.J., Green, D.H., Sie, S.H., 1992. Trace and minor element partitioning between garnet and amphibole and carbonatitic melt. Earth Planet. Sci. Lett. 113, 1–14.

Sweeney, R.J., Prozesky, V., Przybylowicz, W., 1995. Selected trace and minor element partitioning between peridotite minerals and carbonatite melts at 18–46 kbar pressure. Geochim. Cosmochim. Acta 59, 3671–3683.

Thomas, R.J., Agenbacht, A.L.D., Cornell, D.H., Moore, J.M., 1994. The Kibarian of southern Africa — tectonic evolution and metallogeny. Ore Geol. Rev. 9, 131–160.

Thomsen, T.B., Schmidt, M.W., 2008. Melting of carbonated pelites at 2.5–5.0 GPa, silicate–carbonatite liquid immiscibility, and potassium–carbon metasomatism of the mantle. Earth Planet. Earth Planet. Sci. Lett. 267, 17–31.

Ulmer, P., Sweeney, R.J., 2002. Generation and differentiation of group II kimberlites: constraints from a high-pressure experimental study to 10 GPa. Geochim. Cosmochim. Acta 66, 2139–2153.

Van Westrenen, W., Draper, D.S., 2007. Quantifying garnet-melt trace element partitioning using lattice-strain theory: new crystal-chemical and thermodynamic constraints. Contrib. Mineral. Petrol. 154, 717–730.

Veksler, I.V., Petibon, C., Jenner, G.A., Dorfman, A.M., Dingwell, D.B., 1998. Trace element partitioning in immiscible silicate-carbonate liquid systems: an initial experimental study using a centrifuge autoclave. J. Petrol. 39, 2095–2104.

Weaver, B.L., 1991a. The origin of ocean island basalt end-member compositions — trace-element and isotopic constraints. Earth Planet. Sci. Lett. 104, 381–397.

Weaver, B.L., 1991b. Trace-element evidence for the origin of ocean-island basalts. Geology 19, 123–126.

Wood, B.J., Blundy, J.D., 1997. A predictive model for rare earth element partitioning between silicate and anhydrous silicate melt. Contrib. Mineral. Petrol. 129, 166–181.

Yasuda, A., Fujii, T., Kurita, K., 1994. Melting phase-relations of an anhydrous mid-ocean ridge basalt from 3 to 20 GPa — implications for the behaviour of subducted oceanic-crust in the mantle. J. Geophys. Res. 99, 9401–9414.

Yaxley, G.M., Brey, G.P., 2004. Phase relations of carbonate-bearing eclogite assemblages from 2.5 to 5.5 GPa: implications for petrogenesis of carbonatites. Contrib. Mineral. Petrol. 146, 606–619.

Zhang, J., Ko, J., Hazen, R.M., Prewitt, C.T., 1993. High-pressure crystal chemistry of $KAlSi_3O_8$ hollandite. Am. Mineral. 78, 493–499.